Intrinsic properties of nanoparticulate Ir-based catalysts for oxygen evolution reaction by AC voltammetry

Ožbej Vodeb [a,b], Anja Lončar [a,c], Marjan Bele [a], Armin Hrnjić [a,c], Primož Jovanovič [a], Miran Gaberšček [a], Nejc Hodnik [a,b,c,*]

[a] Department of Materials Chemistry, National Institute of Chemistry, Hajdrihova 19, Ljubljana 1000, Slovenia
[b] Jožef Stefan International Postgraduate School, Jamova cesta 39, Ljubljana 1000, Slovenia
[c] University of Nova Gorica, Vipavska 13, Nova Gorica 5000, Slovenia

ABSTRACT

Water splitting in acidic media is a sustainable and efficient new way to produce hydrogen fuel. However, the main bottleneck preventing the wider use of electrolyzers is still the oxygen evolution reaction (OER). Currently, the best electrocatalysts for OER are Ir-based materials, but the mechanistic details are still not fully understood. In this work, we investigate the similarities and differences in the OER mechanism of three different Ir-based catalysts, namely Vulcan carbon-supported and unsupported metallic Ir and rutile IrO_2 nanoparticles, and the process of Ir activation. For this purpose, we use large amplitude AC Voltammetry to distinguish between capacitive and faradaic processes. To quantify the data, we also use a mechanistic fit of the resolved harmonics. We show that all catalysts share the same OER mechanism but require different amounts of activation cycles. We have found three intrinsic properties, which can adequately describe a material for electrocatalysis. First is the activation threshold number (ATN), second is the current normalized to the number of active sites (intrinsic current), and lastly the mass normalized active site density. It was found that Ir on Vulcan has an intrinsic activity at least 3 times higher than the other two materials under consideration, as well as having the highest active site density. From the model fits we can also gain further insight into the mechanistic details for each material. For metallic Ir samples, the rate-limiting step is shown to be water adsorption, whereas for IrO_2 the bottleneck is the inherently slower kinetics. This also indicates that IrO_2 does not produce the same IrOH as Ir metal and therefore has different intrinsic properties. This study provides new insights into the intrinsic properties of different Ir nanocatalysts and highlights a general approach to studying the reaction mechanisms and intrinsic properties of electrocatalysts.

1. Introduction

Proton exchange membrane (PEM) water electrolyzers (WE) are a promising electrochemical system for efficient hydrogen production from renewable energy sources as an alternative to fossil fuels. These devices exhibit three to four times higher current densities compared to alkaline electrolyzers and dynamic operations that allow effective switching between on and off periods, which is unavoidable due to the intermittency of renewable energy sources [1,2]. For PEM-WE, Ir is currently the only viable catalyst for efficient oxygen evolution reaction (OER), which is the kinetic bottleneck of the acidic water splitting process. Therefore, such a device is currently a sound choice if dynamic and effective energy conversion is the only criterion. However, from an

economic point of view, the need for noble metals is a major drawback, mainly because Ir is a very scarce and extremely expensive metal, and therefore classified as a critical raw material. Only 10 tonnes of Ir are mined per year which will soon become a major problem if hydrogen production targets in the order of 100 GW of electrolyzer capacity are to be met (e.g., 2030–2050) [3]. To a large extent, the problem of Ir utilization can be remedied by using Ir nanoparticles, as this reduces the amount of Ir, and also expands its catalytic surface area. Nevertheless, due to the extremely low availability of Ir, this is still not a sufficient solution for fast mass commercialization of polymer electrolyte membrane electrolyzer technology [1,2,4].

There have been many fundamental studies published on the topic of electrochemical properties of Ir as an oxygen evolution reaction (OER)

catalyst, studied mostly on model systems [5–10]. For bulk Ir electrodes, it has been shown that activation via electrochemical cycling continuously produces more and more porous Ir hydrous oxide (IrOH), which acts as an active site for OER. Many studies, summarized in several reviews [5,6,11,12], have been dedicated to hydroxide formation and its effect on OER. In essence, by cycling bulk Ir material between a low and high voltage (usually between approximately 0 V and 1.5 V vs. RHE) the surface of Ir starts to irreversibly oxidize and thus restructure (e.g., formation of cracks) into a porous gel-like structure, referred in the literature as a 3D catalyst. This is seen as substantial growth of capacitive current with every cycle in cyclic voltammetry. This repetitive oxidation and reduction changes not only the morphology of Ir surface but also its electrochemical intrinsic properties, namely the electrochemically active surface area and the formation of specific OER active sites (turnover frequency) [5,6].

Recently, Krewer et al. [13,14] employed a combined theoretical-experimental approach to study the OER mechanisms on different Ir systems. They fitted a microkinetic model based on DFT calculations to the measured cyclic voltammograms (CVs) of bulk Ir electrodes and IrO$_2$ nanoparticles. Their works showed that essentially all Ir-based catalysts share the same reaction pathway for OER.

Despite decades of fundamental studies on Ir electrocatalysis, not much work on understanding the Ir hydroxide formation has been done on Ir nanoparticles. Preparing various forms of Ir nanoparticulate catalysts, which can differ in many physical properties, comes with some lingering questions that are still not fully addressed in the literature. For example, how do the support and oxidation state of Ir affect the intrinsic properties of these Ir catalysts? Do different Ir-based catalysts need different activation treatments before reaching an active state? Do all Ir-based nanoparticles exhibit the same OER mechanism and possess the same intrinsic properties?

Voltammetric methods that are based on large amplitude alternating current (ACV) usually include a potential procedure where a sine wave of known frequency and amplitude is added to the conventional procedure of linear sweep or cyclic voltammetry experiment. With a sufficiently large amplitude, harmonics higher than the base frequency will occur. To date, the method has been applied in various fields of electrochemistry [15,16]. Major advances and applications have been made by Bond et al. [15–18]. In particular, when the method is combined with a model-experiment comparison approach, it can prove to be a particularly powerful tool for understanding the electrochemical phenomena that occur on a catalyst surface [15,18,19]. This method can in principle effectively distinguish between Faradaic and capacitive currents, as harmonics are a consequence of only electrochemical reactions. These harmonics can then be filtered using the Fourier transform (FT). By analyzing the harmonics, the electrochemical reactions occurring on the Ir surface can be elegantly separated and thus analyzed. Such an analysis can provide a basis for discussion of the reaction pathway and intrinsic properties for different catalysts, such as supported Ir nanoparticles. On the contrary, conventional cyclic voltammetry is in most cases unable to distinguish between different electrochemical processes.

In this work, we employ ACV to investigate how oxidation state of Ir and support affect the intrinsic catalytic properties of Ir-based nanoparticles. We use three different Ir-based nanoparticulate materials, namely unsupported Ir particles, i.e., Ir Black, rutile oxide IrO$_2$, and Ir particles, supported on a Vulcan carbon. We perform ACV measurement and analyze the obtained ACVs for each material before and after a series of potentiodynamic cycles. By comparing the measurements for different materials, we were able to track how the mechanism and properties of each material change as the number of activation cycles increases and how long it takes the material to reach a steady state, i.e., the activation threshold number. We performed a simulation to mechanistically fit the experimental results of AC voltammetry for each of the most active states of the materials. From this, OER mechanistic differences and similarities among the materials are inferred and the hypothesis that all Ir-based materials essentially share the same

mechanistic pathway is tested.

2. Experimental

2.1. Materials and electrochemical characterization

Several materials with supported and unsupported Ir-based nanoparticles were used. Two commercial samples, namely Ir Black (Alfa Aesar) and Ir on Vulcan (20% Ir, Premetek) were compared to in-house synthesized IrO$_2$ nanoparticles.

Iridium oxide nanoparticles were prepared by thermal treatment of an iridium precursor in a silica template, which was subsequently removed. For this purpose, 0.4 g iridium(III) bromide hydrate (Sigma-Aldrich) was first dissolved in 10 mL of water at 50 °C. The solution was then mixed with 3 g of fumed silica (Cab-O-Sil M-5, Cabot Corporation) at 50 °C until evaporated (lightly ground in a mortar). The mixture was then thermally treated in air, raising the temperature to 500 °C at a rate of 2 °C per minute for 10 h, and then cooled to room temperature. The silica matrix was then removed from the thermally treated mixture by first dissolving it in 60 ml of 6 M NaOH at 60 °C and followed by centrifugation at 7000 rpm for 15 min and washing with water four times. Preparing the oxide material in this way allows better control of nanoparticle size. X-ray spectra and sample analysis are available in Supplementary Materials Section 1.

All electrochemical measurements were performed in a standard glass cell with three electrodes and a Biologic SP-300 potentiostat. The electrodes used were a graphite counter electrode, a HydroFlex reversible hydrogen electrode (RHE) (Gaskatel GmbH) reference electrode, and glassy carbon (GC) rotating disc electrode (RDE) from PINE as a working electrode, to which thin films of the investigated materials were deposited by drop casting. All potentials are given against RHE. Before the experiment, the cell was boiled in distilled water for 1 h and then thoroughly rinsed with Milli-Q water (18.2 MΩ cm). To ensure maximum purity of the working electrodes, the GC discs were polished with an alumina suspension (0.05 μm, MasterPrep, Buehler) and afterward washed by sonication in water for 5 min three times. The electrodes were then rinsed with water and dried under N$_2$ atmosphere. For the deposition of thin films on RDEs, suspensions containing different concentrations of Ir-based samples were prepared by weighing a material on a mg scale and then adding a suitable amount of water. In addition, a Nafion stock solution (Aldrich) was added to the suspension so that the amount of Nafion was 25 wt% of the solid content in the suspension. The ink was homogenized by sonication in an ice bath with a sonication horn (4 s pulse, 2 s pause) for 20 min. The prepared suspension was drop cast onto a clean and dry working electrode, which was then left to dry overnight in a closed plastic desiccator.

Hydrous Ir oxide films were prepared by 100, 200, 500, and 1000 square wave pulses (SQW) between 0.05 and 1.45 V (2 s steps). The supporting electrolyte was 0.1 M perchloric acid (HClO$_4$, 70% Rotipuran Supra, Carl Roth, diluted with water). ACV and LSV scans were performed before and after each set of cycles. The ACV scans were performed at a scan rate of 1 mV/s from 0.4 V to 1.5 V. The sine wave was constructed with a frequency of 0.127 Hz and an amplitude of 150 mV. This provided a sufficient signal-to-noise ratio. The harmonics were filtered out as discussed in the literature [15]. A potential window between 0.4 V and 1.6 V was used for the LSV scan, with a scan rate of 5 mV/s.

2.2. Model

The model used in our kinetic study is the one reported in previous articles [13,14]. They constructed a model based on DFT calculations performed by other groups and linked the calculations to experimental findings. The proposed mechanism is composed of four electrochemical and three chemical steps. The first reaction step is a chemical one representing the adsorption of water on the electrode (denoted as C1). This

is followed by two electrochemical deprotonation steps (E1 and E2), a chemical water adsorption step (dubbed C2), and the last two electrochemical deprotonation steps (E3 and E4). All the steps described are connected by the final chemical step of oxygen desorption which completes the reaction cycle (C3).

We believe that the active site in this reaction, denoted as "*", is always an exposed Ir atom found on the surface. Nevertheless, the kinetics of an active site is not only influenced by the atom on which a reaction occurs but also by the atom's surroundings, therefore different kinetic parameters are expected for the metallic and oxide materials. On the surface of metallic Ir samples, the formation of an amorphous hydrous oxide is expected to form, while for the oxide sample electrocatalysis is performed on a crystalline surface. We also expect some parameter dispersion to occur, as the nanoparticles in our samples do not have a uniform surface and should show different behavior. This fact should arise from non-conformity between the different harmonic fits, thus showing a harmonic dependence of some of the fitted parameters, as our model does not encapsulate the frequency dependence of our parameters. This is further discussed later in the article.

$$* + H_2O \rightleftharpoons H_2O^* \tag{C1}$$

$$H_2O^* \rightleftharpoons OH^* + H^+ + e^- \tag{E1}$$

$$OH^* \rightleftharpoons O^* + H^+ + e^- \tag{E2}$$

$$O^* + H_2O \rightleftharpoons OH_2O^* \tag{C2}$$

$$OH_2O^* \rightleftharpoons OOH^* + H^+ + e^- \tag{E3}$$

$$OOH^* \rightleftharpoons OO^* + H^+ + e^- \tag{E4}$$

$$OO^* \rightleftharpoons O_2 + * \tag{C3}$$
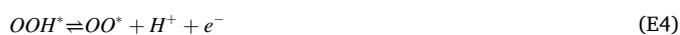
The C and E steps were converted into a set of ordinary differential equations (ODEs), which can be found in Supplementary Materials Section 2 (S1-S7). To fully describe the kinetic model, each electrochemical step requires a set of three constants, while chemical steps are described with a single constant describing one direction of a reaction. In addition, the total number of active sites is also required to solve these equations. Finally, equations describing the double-layer charging (C_{dl}) and the voltage drop due to uncompensated resistance (R_u), as well as the faradaic current were included in the model. To calculate these effects, we employed equations S8-S10, also found in Section 2 of Supplementary Materials.

While the mechanistic steps are the same as in the above mentioned studies, the mathematical formulation in this article differs from that in the previous ones [13,14]. In our study, we used the Butler-Volmer formalism to describe electrochemical reactions and the adsorption isotherm used was Temkins' instead of the van der Waals' isotherm as reported in the cited articles. We have tested the use of the Temkin isotherm by fitting the peak at 1.01 V and we found that it fits the peak better than any other isotherm. The use of the Temkin isotherm also simplifies the numerical procedure, making the algorithm somewhat faster. The algorithm uses 26 constants to create simulated data. To find these constants a fit was made for the respective harmonic currents of each material. The constants used to fit the model are found and explained in the Supplementary Materials (Sections 2 and 3). We give a brief glossary of the constants in Table 1.

To solve the set of ODEs, an implicit discretization was used for the time step. The resulting set of algebraic equations was then calculated by using the hybrid method found in the "root" routine of SciPy [20], where the parameters of the method are the default settings. This way, using the potential given by the potentiostat, the current for each time step could be calculated. The "curve_fit" routine included in Python's ScyPy module was used to fit each harmonic separately. The tolerance for the fit was set to 10^{-8}. The routine also provides information about the

Table 1

A quick glossary of the constants used to describe the mathematical model.

Constant	Description
$\alpha_1, \alpha_2, \alpha_3, \alpha_4$	Charge transfer coefficients, corresponding to the E1, E2, E3, and E4 steps
$E_{0,1}; E_{0,2}; E_{0,3}; E_{0,4}$	Formal potentials for the E1, E2, E3, and E4 steps
$k_{0,1}; k_{0,2}; k_{0,3}; k_{0,4}$	Rate constants for the electrochemical E1, E2, E3, and E4 steps
k_{ad1}, k_{ad2}	The forward and backward constant for the initial adsorption step (C1)
k_{c1}, k_{c2}	The forward and backward constant for the second chemical step (C2)
k_r	The rate constant describing the step of oxygen desorption (C3)
n_0	The total number of active sites
$S_*, S_{H2O}, S_{OH}, S_O, S_{OH2O},$ S_{OOH}, S_{OO}	Temkin isotherm constant for each species
C_{dl}	Double layer capacitance

standard deviation of each parameter from which the confidence region can be estimated as discussed in reference [21]. A relative root mean squared error (RRMSE) comparison function between the simulated and experimental harmonic data was used to evaluate the "goodness of fit".

3. Results and discussion

3.1. Characterization/comparison of materials

In this study, we compare three of the most common high surface area Ir nanomaterials for OER. These are Ir Black, Ir on Vulcan and rutile IrO_2. All three materials are composed of nanoparticles, where Ir Black and Ir on Vulcan consist of metallic Ir nanoparticles, with the difference that in Ir on Vulcan Ir nanoparticles are dispersed over a high surface area Vulcan carbon support. IrO_2 are oxide nanoparticles with a rutile structure prepared by annealing in a silica matrix, which was later removed by dissolution. Fig. 1 shows TEM images as well as the particle size distribution obtained from the TEM images for each material. From the images, it can be seen that both Ir black and IrO_2 are agglomerated, while Ir on Vulcan shows a dispersion of smaller nanoparticles on the support but also contains some agglomerates. The average particle size for each material is 2.64 nm for Ir Black, 2.1 nm for Ir on Vulcan and 7.4 nm for IrO_2 nanoparticles.

Until now, fundamental studies have been performed mostly on bulk Ir metal electrodes [11,12,14,24–26], while studies on the basic OER mechanism on nanosized Ir catalysts are lacking. For bulk Ir metal, three steps associated with the oxidation of the Ir surface are believed to occur prior to the onset of OER at about 1.4 V. Below (Fig. 2) we show how LSV curves for our Ir samples change with cycling. Looking at the Figure, we see that the first peak is seen at about 0.6 V, another at about 0.9 V and the last of the three peaks at about 1.3 V. These peaks correspond to reaction steps E1, E2, and E3, respectively. In bulk Ir, growth of IrOH was also observed when the material was cycled between a higher and lower potential [12,23]. Based on this we hypothesize that the processes should be similar for nanosized Ir.

The LSV curves show that the material undergoes some changes during cycling, which we refer to as activation. On a bulk Ir sample, this process is associated with the extensive growth of 3D hydrous-oxide (IrOH). It has been observed in numerous studies by examining the voltammetric behavior of Ir [5,6,12], and studying the catalyst surface by spectroscopic methods [25–27]. The behavior of nanosized particles resembles that of bulk Ir but with some distinct differences. It can be observed that, even after activation, Ir on Vulcan exhibits poorly defined peaks at potentials where one would expect an Ir oxidation/reduction reaction (Fig. 2c, looking at potential ranges from 0.8 V to 1.3 V). While this can be also said for IrO_2 and Ir Black samples, they nonetheless have better-resolved peaks (Fig. 2a for Ir Black and 2e for IrO_2). Using the LSVs, we can also see that the potentials at which we see these peaks are
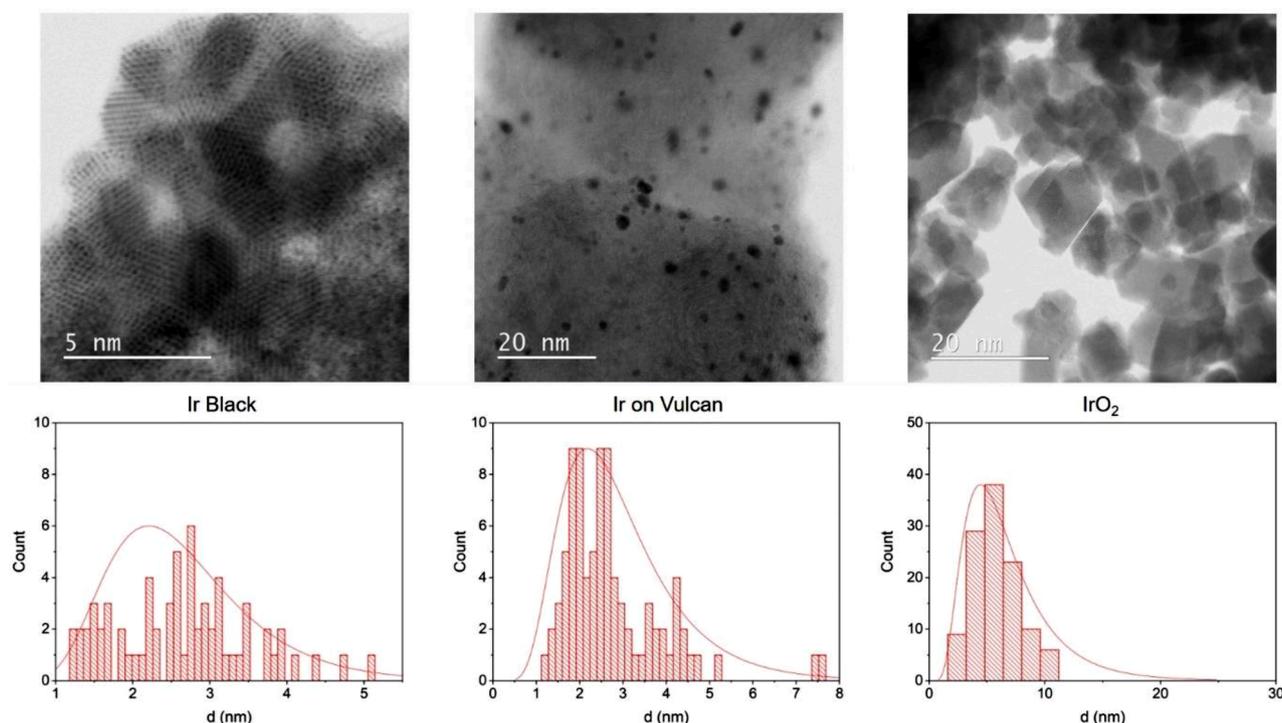
Fig. 1. TEM images and particle size distributions for the studied materials. In order from left to right: Ir Black, Ir on Vulcan and IrO$_2$.

higher than those reported for bulk Ir [5,6,12,22–24]. Most striking is the peak at 1.01 V, which in the case of bulk Ir would correlate with a peak at 0.9 V whereas the peak shape for nanosized Ir appears to be much broader. These differences may be attributed to the fact that IrOH forms differently on our different Ir-based nanostructures. We hypothesize that this depends on the nature of the support and the oxidation state of Ir.

Looking at the general shape of LSVs in Fig. 2, we believe that the underlying nature of reactions and mechanisms are the same regardless of whether the material is a supported Ir nanoparticle, bulk Ir, or even IrO$_2$. Nevertheless, some distinct differences should be further analyzed as they might affect the intrinsic properties of Ir OER. To better understand the similarities and differences between the materials, we employed the ACV method and examined the different materials at different stages of activation. This allowed us to more accurately identify the faradaic peaks and thus track the changes of the materials through the activation or even degradation with cycling. Fig. 3 illustrates how ACV can better show electrochemical reactions, compared to a LSV/CV. We speculate that the way a material activates is dependent on the material's initial structure and oxidation state, that is pure metallic Ir or a thermally prepared oxide.

3.2. ACV voltammograms/harmonics and their interpretation

Looking at the ACV scans for different materials we find that different material configurations, where Ir is supported or unsupported and the oxidation states of Ir are different, indeed affect a material's activation process (Fig. 4). From the plots, it can be seen that some materials reach a steady state more quickly, notably seen in Fig. 4a, c, and e.

In our study, we focus on the 3rd harmonic onward, as the lower harmonics have a noticeable contribution from ringing (Supplementary materials Section 5). This noise arises due to the numerical procedure used when filtering the harmonics in the frequency domain and we have been unable to avoid it for the 0th, 1st, and 2nd harmonic. The contribution from ringing becomes less noticeable for the higher harmonics, however noticeable contribution arises due to white noise in the 8th

harmonic onward. As such the 3rd and 4th harmonic are of primary concern in this study as they have the cleanest data set. The authors however would like to stress that all harmonics share the same basic information.

Based on these results, we can attribute to each material its own activation threshold number (ATN). This can be seen as the harmonic currents begin to converge to a final shape that does not change with continued cycling, shown in Fig. 4a, c and e. We observe that only the current amplitude increases or decreases, indicating that we are observing the profile of a particular material, whose quantity (amount) is increasing or decreasing. Ir Black and Ir on Vulcan are the fastest, requiring only 100 cycles to reach a steady state, which is consistent with our previous observations where we confirmed this only with CV [28,29]. Moreover, subsequent cycling only contributes to the decrease in current amplitude. IrO$_2$ is the slowest to fully activate, requiring 1000 cycles to reach the final steady state. Based on these trends, we can already see that Ir-based metallic analogues behave similarly, while rutile Ir oxide behaves differently. This is summarized in Table 2. To further support this claim, a more thorough investigation of the OER pathway was performed.

Let us focus our attention exclusively on the shape and location of the peak of the 3rd harmonic (as shown in Fig. 4) and disregard the amplitude of the current. For potentials up to 1.3 V, we can observe that the harmonic voltammograms for both metallic Ir catalysts reach similar shapes after ATN of cycles, namely a steady state, seen in Fig. 4a and c. The harmonic voltammogram for IrO$_2$ (Fig. 4e and f) show some important similarities with the metallic Ir-based samples. Most notable is the fact that the peaks occur at similar potentials for the supported Ir. At the end of activation, when ATN is reached for each material, the peak potentials for supported Ir and IrO$_2$ are virtually the same. This fact supports the original hypothesis that Ir-based materials have the same reaction pathway. However, Fig. 4e shows that the shape of the peaks of IrO$_2$ is quite different from that of metallic Ir materials. This suggests that the surface of IrO$_2$ has evolved differently than that of Ir metal. This will be further substantiated in the next section, where the mechanistic details will be presented. On this basis, we conclude that all three studied materials have the same mechanistic pathway, i.e., the same
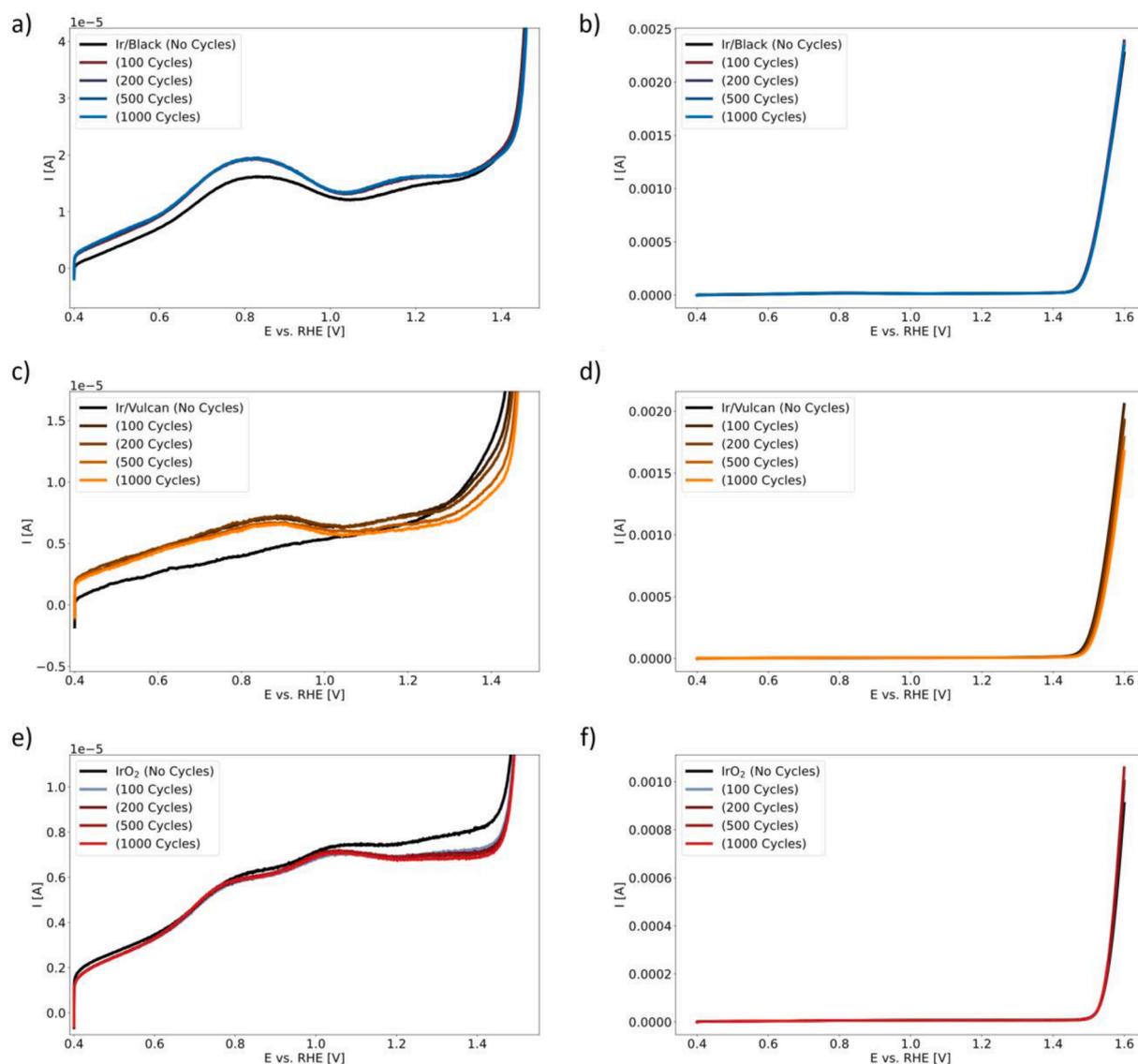
Fig. 2. LSV comparison between the different Ir catalysts. From top to bottom: Ir Black, Ir on Vulcan and IrO$_2$. Fig. 2a, c and e show a close up of the region between 0.4 V and about 1.45 V in the Fig. 2b, d and f. LSV scan from 0.4 V to 1.6 V was performed in 0.1 M HClO$_4$ for each material as deposited and after 100, 200, 500 and 1000 cycles. The materials were cycled by squared wave pulses, switching between 0.05 V and 1.45 V, with a potential hold of 2 s for each potential. All potentials are given with respect to the RHE reference electrode.
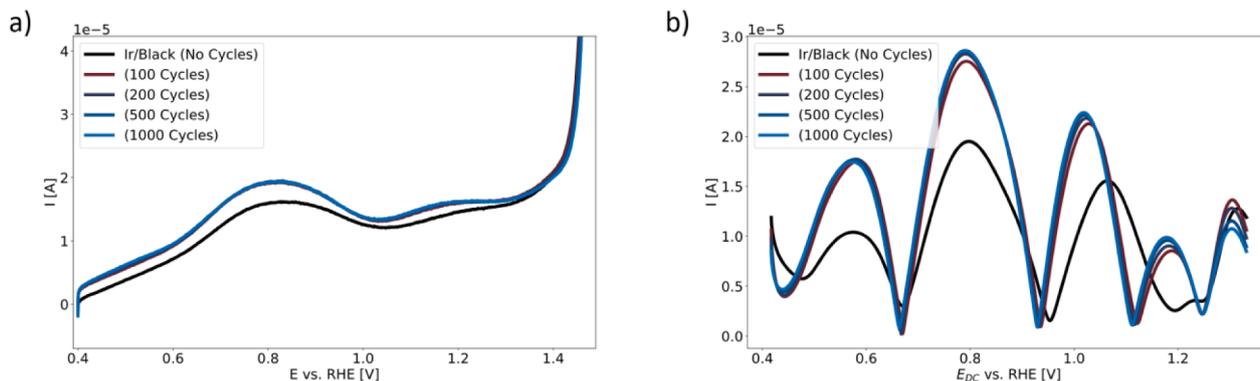
Fig. 3. Comparison between LSV (3a) and 3rd harmonic (3b) for Ir Black. Fig. 3 represents the advantage ACV has over cyclic voltammetry, as now electrochemical reactions can be seen in more detail. LSV and ACV measurements are taken before and after 100, 200, 500 and 1000 cycles of square wave pulses between 0.05 V and 1.45 V with a 2 s potential hold. The LSV was performed between 0.4 V and 1.6 V with a scan rate of 5 mV/s and the ACV scan made between 0.4 V and 1.5 V, with a scan rate of 1 mV/s, with a frequency and amplitude of 0.127 Hz and 150 mV respectively. All experiments are made in 0.1 M HClO$_4$ acid and all potentials are measured versus RHE.
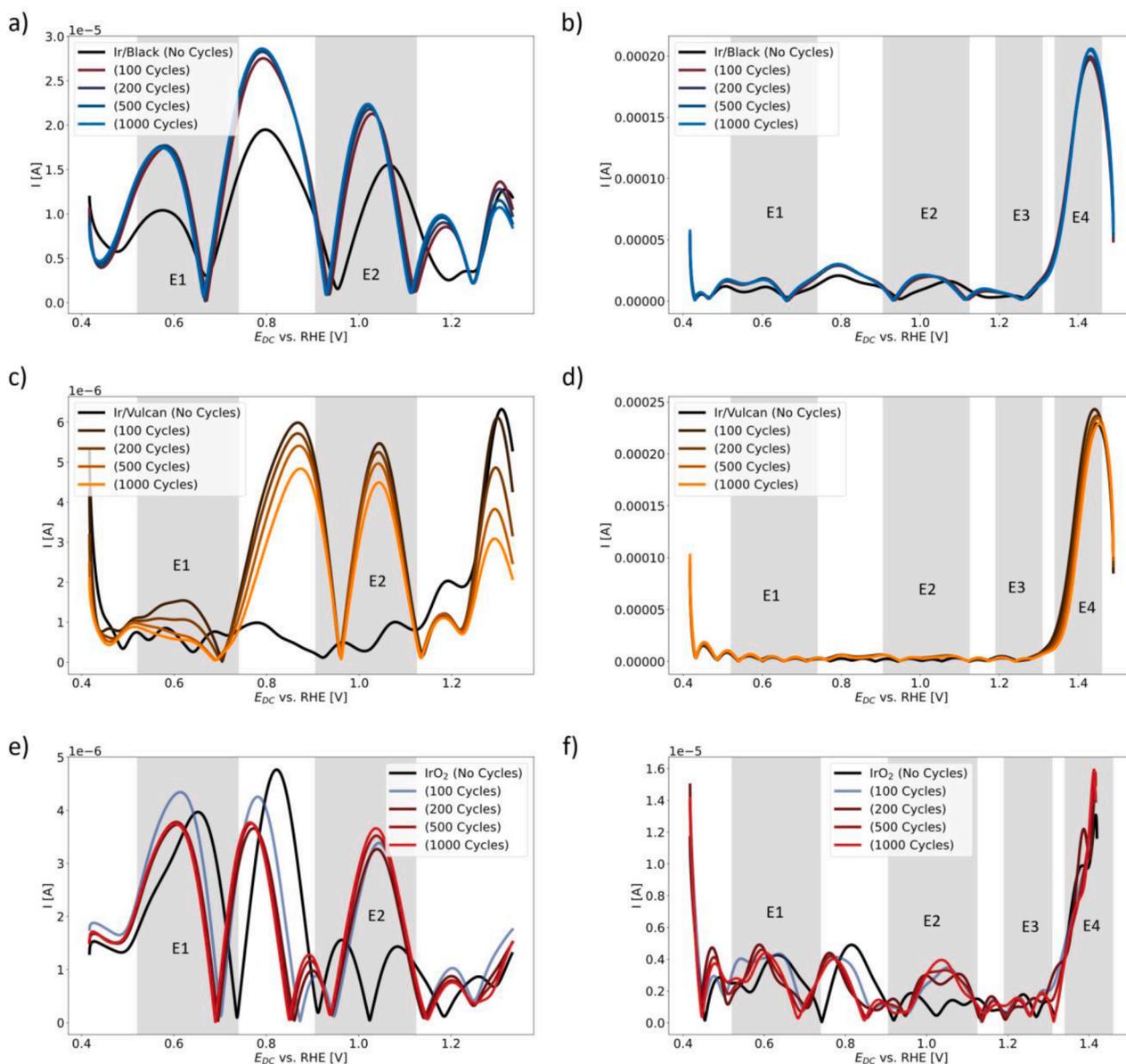
Fig. 4. 3rd harmonic comparison for the studied materials. From top to bottom: Ir Black, Ir on Vulcan and IrO$_2$. Fig. 4a, c, and e show a close-up of the region between 0.4 V and 1.3 V of Fig. 4b, 4d, and f. In Fig. 4a–f, E1, E2, E3, and E4 note the electrochemical steps described previously in the text. The rest of the harmonics can be found in Supplementary Materials section 5. The ACV scans were made in 0.1 M HClO$_4$. The potential range was from 0.4 V and 1.5 V with a scan rate of 1 mV/s. The frequency was 0.127 Hz and the potential amplitude was 150 mV for the sinusoidal part of the signal. All potentials are with respect to the RHE.

intermediate stages.

While the general peak shape and position are virtually identical, some differences are apparent when considering the non-primary peaks of the odd harmonics (see Supplementary Materials Section 5). This means that the reaction kinetics are different for different materials. To fully understand the reaction kinetics a comparison between the model (described above) and the experiment is required.

3.3. Discussion on oer mechanism fits

To further verify whether all of the materials truly share the same reaction pathway, we fitted the measured data with the model presented previously in the text. This way we can directly detect and confirm the differences and similarities among the materials. We performed the fits to the ACV after ATN of cycles, which we considered to be the steady states. By doing this we can determine the relevant kinetic parameters used to describe the kinetic model, as well as the number of active sites

for each material. If the model fits the experimental data correctly we would expect to find a similar set of parameters at each frequency, whether that response is a consequence of the input signal or a harmonic current. We rely on the ACV method after filtering the harmonics to provide us with data, as using such a method minimizes the contribution from non-Faradaic sources and the resulting signal's source is solely a contribution from electrochemical reactions on the surface. However, some kinetic parameters can exhibit a frequency dependence and there is a likelihood that it may also appear in our study. For this reason, we have fitted each of the studied harmonics separately to further validate our model and see if any of the parameters fitted show a frequency dependence. A quick glossary of the fitted constants is available in Table 1, as well as in Supplementary Materials Section 2.

Based on the data fit, we can see that the proposed mechanism adequately reflects the obtained ACV data. The example below shows the fit to the 4th harmonic for each material after ATN (100 cycles for Ir Black and Ir on Vulcan and 1000 cycles for IrO$_2$). The rest of the fits and
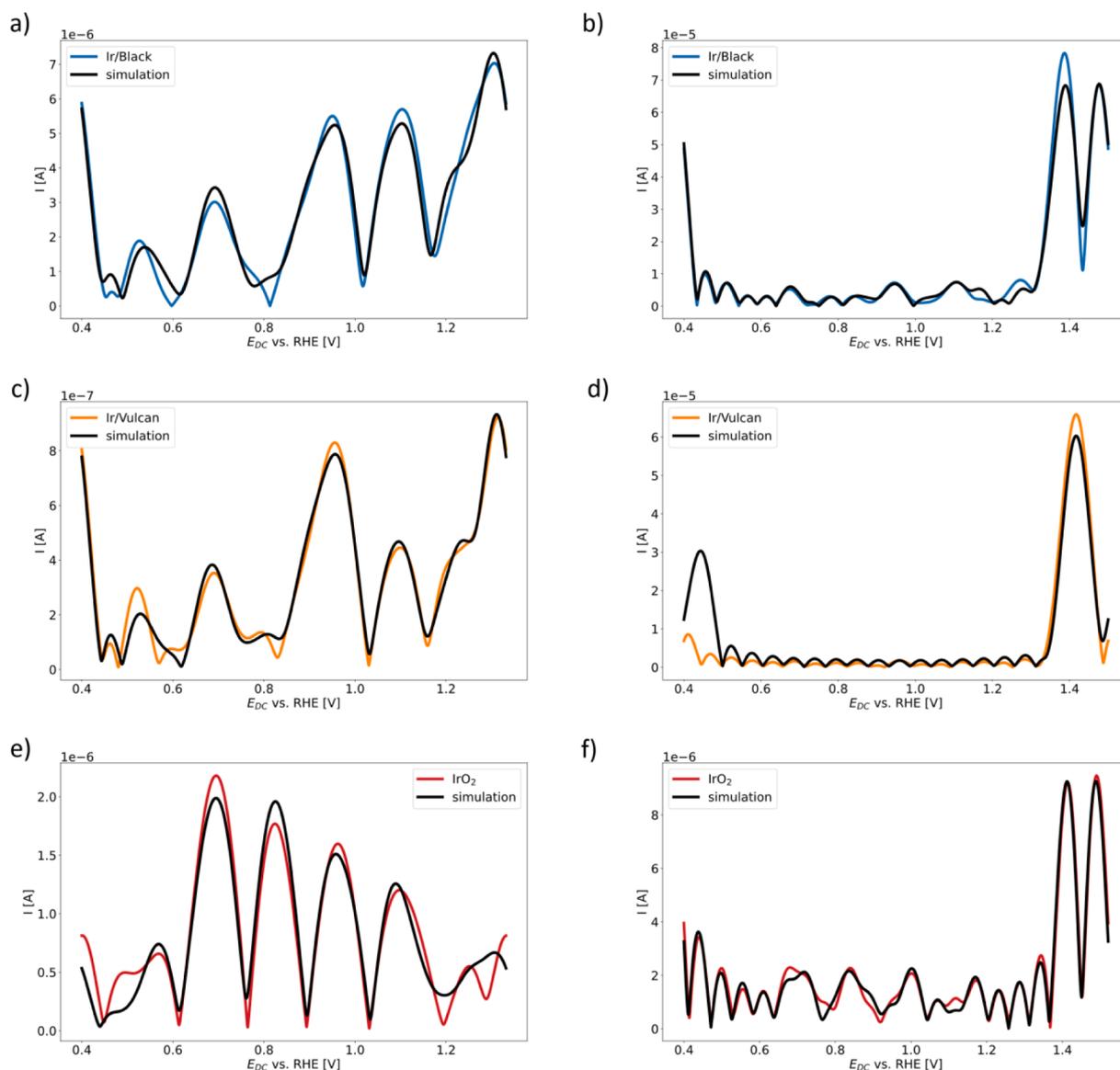
Fig. 5. Comparison between simulation and experiment for the 4th harmonic currents after activation (100 cycles for Ir Black and Ir on Vulcan and 1000 cycles for IrO$_2$) for each studied material. From top to bottom: Ir Black, Ir on Vulcan and IrO$_2$. Fig. 5a, c, and e show the region between 0.4 V and 1.3 V for the Fig. 5b, d, and f in more detail. The experimental ACV was made with the linear ramp going from 0.4 V to 1.5 V with a scan rate of 1 mV/s, the sinusoidal signal has a frequency of 0.127 Hz and an amplitude of 150 mV. The measurement was made in 0.1 M HClO$_4$. All potentials are reported versus RHE.

Table 2

ATN for the materials studied. Square-wave pulses (SQW) between 0.05 and 1.45 V were used for the cycling protocol and each potential was held for 2 s. ACV measurements were performed after 100, 200, 500, and 1000 cycles.

Material	Activation threshold number
Ir Black	100
Ir on Vulcan	100
IrO$_2$	1000

their confidence limits are available in Supplementary Materials Section 6 for this article. From the "goodness of fit" parameter for each harmonic we can see that all fits are indeed adequate. Below we treat the confidence limits for our parameters in a quantitative manner and provide further discussion on the adequacy of the model fit.

There is a consistency among the fits when observing the confidence limits for each parameter. It shows that the confidence limit for the formal potentials (E$_0$) and charge transfer coefficients (α) are very narrow, thus showing that the found parameters are likely correct. The confidence limits for the isotherm constants (denoted as S$_x$, with x as a stand-in for a species name) vary between the species, most of them have a narrow region, thus showing their importance to the model, with the constants for the active site (S$_*$), initially adsorbed water molecule (S$_{H2O}$), and finally, the final oxygen molecule (S$_{OO}$) having a wide confidence region. This could be the consequence of cross-correlation with kinetic parameters, as can be seen from the confidence regions for the kinetic parameters, as here the kinetic constants for the first and last electrochemical reactions (k$_{0,1}$ and k$_{0,4}$) have wide confidence regions. However, observing the confidence regions for the second and third kinetic constants (k$_{0,2}$ and k$_{0,3}$), the regions are relatively narrow, thus justifying the use of the Temkin isotherm at least for these two reactions. The kinetic parameters for the initial adsorption step (k$_{ad,1}$ and k$_{ad,2}$) again show a large confidence region, which again can be explained with correlation with the isotherm term in the equation. The C2 (k$_{c,1}$ and k$_{c,2}$) step has a much narrower confidence region, showing

that the found parameters are likely correct, with the equilibrium being pushed in the forward direction in all cases. The parameter for the number of active sites (n_0) shows a narrow confidence region, along with the double layer capacitance (C_{dl}), however, some doubt can be given to the found double layer capacitance found in the higher harmonics (5th onward), as the contribution from double layer charging is minimal in these harmonics. These results show that while some doubt can be given to some parameters from the individual harmonic fits, our confidence in the found harmonic fits is sufficient for us to accept the exercise on an individual basis. However, a problem of the current model is the inconsistency between the harmonic fits. In a perfect scenario, the correct model should exhibit consistency through all of the harmonic fits. We provide more discussion of this fact later in the article.

After justifying the correctness of the fit, we can now concentrate on the results, i.e. the obtained constants, collected in Table 3. Literature reports suggest a redox potential window for Ir from 0.8 V up to 1.3 V, where Ir undergoes a change in the oxidation state [5,6,30,31]. This is in line with our reports of formal potentials for the reactions E1, E2, and E3, which have values of 0.9 V, 1.1 V, and 1.3 V respectively for the metallic samples. Rutile IrO_2 however shows a slight deviation, with formal potentials 0.83 V, 1.1 V, and 1.4 V respectively for the stated reactions. Due to the nature of cyclic voltammograms for Ir nanoparticles seldom showing well-resolved peaks, it is difficult to make good comparisons with the obtained formal potentials. However, for metallic samples, it can be seen with ACV (Fig. 4), that the first redox step occurs at around 0.9 V, with the second following at roughly 1.1 V, which is in good agreement with our findings (Table 3). The rest are harder to obtain, as the current starts to rise to a degree that there is little certainty in evaluating formal potentials from experimental data. For the oxide sample, it can also be seen that the first step occurs at lower potentials than that of metallics, which is also confirmed by the voltammograms found in the literature [5,6,13,30,31].

We first provide a discussion on the metallic samples (i.e. Ir Black and Ir on Vulcan). From the k_0 constants obtained from the fit, we can see that all four electrochemical steps are indeed quite fast, which means that kinetics is not the limiting factor in OER. The main factor contributing to the distorted peak shape is actually the adsorption isotherm

because if we look at the isotherm constants found, we can see that the first step in the mechanism, i.e., water adsorption, is impeded by the adsorption isotherm, which can be seen from the high values of S_* and S_{H2O}. High values are also observed for the adsorbed single oxygen atom (S_O) and later for the adsorbed oxygen molecule (S_{OO}).

The kinetics at IrO_2 show somewhat different behavior. Here we see that most species are not hindered by adsorption, but that the mechanism is slower due to inherently slower kinetics. This is evident when examining the constants responsible for adsorption kinetics and the chemical step between steps E2 and E3, as the constants $k_{0,2}$ and $k_{0,3}$ for IrO_2 are at least an order of magnitude smaller. It can also be seen that the $E_{0,3}$ value for the E3 step is higher than that of metallic Ir nanoparticles, making the reaction less favorable on IrO_2 than on IrOH grown from Ir metal [32]. This also shows that IrO_2 does not produce the same IrOH as Ir metal and that the material formed in a steady state is somewhat different, as the found constants would otherwise have a similar trend as metallic samples.

Having gained some mechanistic insight, we can now use this knowledge to make simple comparisons between materials and further distinguish them. One of the fitted constants was the number of active sites, an important measure for any study of catalytic materials. Using this number, we can both estimate the active site density based on the catalyst's mass and normalize the polarization curves to gain insight into which material has the highest activity per active site (Fig. 6c and d). Such normalization is a much better way to distinguish between the intrinsic properties of different materials, since we do not need to define what an active surface area is and how it is defined.

The intrinsic activities thus measured are 1.7 mA/nmol for Ir/Black, 5.1 mA/nmol for Ir on Vulcan, and 0.9 mA/nmol for IrO_2. These activities are taken at the OER onset potential of 1.55 V. As such, we can see that Ir on Vulcan is roughly 5.6 times more active than IrO_2, and roughly 3 times more active than Ir/Black. However, a good catalyst should also have a sufficient number of active sites per mass, and the activity of the active sites of a catalyst should not be the only criterion by which we select the best catalyst. Thus, the best of the three catalysts studied would also be Ir on Vulcan, which has an active site density of 0.125 nmol/µg, and is also the most active. The other two materials have an

Table 3
Fitted constants obtained from the 4th harmonic, with the standard deviation of the fit and the calculated RRMSE between the experiment and simulation. A glossary of the constants is available in Table 1.

Constant	Ir/Black	Confidence limit	Ir onVulcan	Confidence limit	IrO_2	Confidence limit
α_1 [/]	0.60	±0.014	0.85	±0.03	0.57	±0.01
E_{01} [V]	0.899	±0.001	0.911	±0.004	0.83	±0.0002
k_{01} [m/s]	12.0	±0.2	10.0	±1.5	3.69	±0.001
k_{ad1} [/s]	107	±3.0	64.7	±8.0	0.33	±0.01
k_{ad2} [/s]	26.3	±0.5	14.2	±1.7	15.6	±0.0001
α_2 [/]	0.426	±0.003	0.58	±0.01	0.47	±0.01
E_{02} [V]	1.160	±0.002	1.12	±0.01	1.11	±0.0004
k_{02} [m/s]	1.47	±0.06	1.08	±0.05	0.71	±0.01
α_3 [/]	0.37	±0.01	0.36	±0.01	0.35	±0.01
E_{03} [V]	1.330	±0.001	1.31	±0.01	1.41	±0.003
k_{03} [m/s]	1.41	±0.02	1.53	±0.09	0.35	±0.01
k_{c1} [/s]	157.0	±5.5	116.0	±12.8	0.006	±0.001
k_{c2} [/s]	15.2	±0.6	21.6	±2.3	0.001	±0.001
α_4 [/]	0.39	±0.03	0.61	±0.04	0.92	±0.01
E_{04} [V]	1.540	±0.006	1.49	±0.18	1.54	±0.08
k_{04} [m/s]	2080	±1020	0.25	±0.21	984	±4340
k_r [/s]	2.11	±0.41	9.01	±70.70	11.0	±9.5
S_* [/]	7.29	±0.16	10.3	±1.6	0.363	±0.001
S_{H2O} [/]	7.12	±0.12	9.42	±0.84	10.13	±0.001
S_{OH} [/]	2.52	±0.12	1.8	±0.1	0.244	±0.002
S_O [/]	0.789	±0.039	1.82	±0.10	1.16	±0.01
S_{OH2O} [/]	8.06	±0.53	15.6	±3.8	0.111	±0.002
S_{OOH} [/]	0.040	±0.001	0.009	±0.002	1.06	±0.01
S_{OO} [/]	20.1	±0.1	13.4	±2.6	1.75	±0.01
n_0 [/]	8.6E-10	±1.1E-11	1.0E-10	±3.5E-12	2.3E-10	±1.4E-12
C_{dl} [F]	5.0E-06	±3.0E-07	6.6E-06	±4.8E-07	3.3E-05	±1.1E-05
RRMSE [/]	0.122		0.103		0.131	
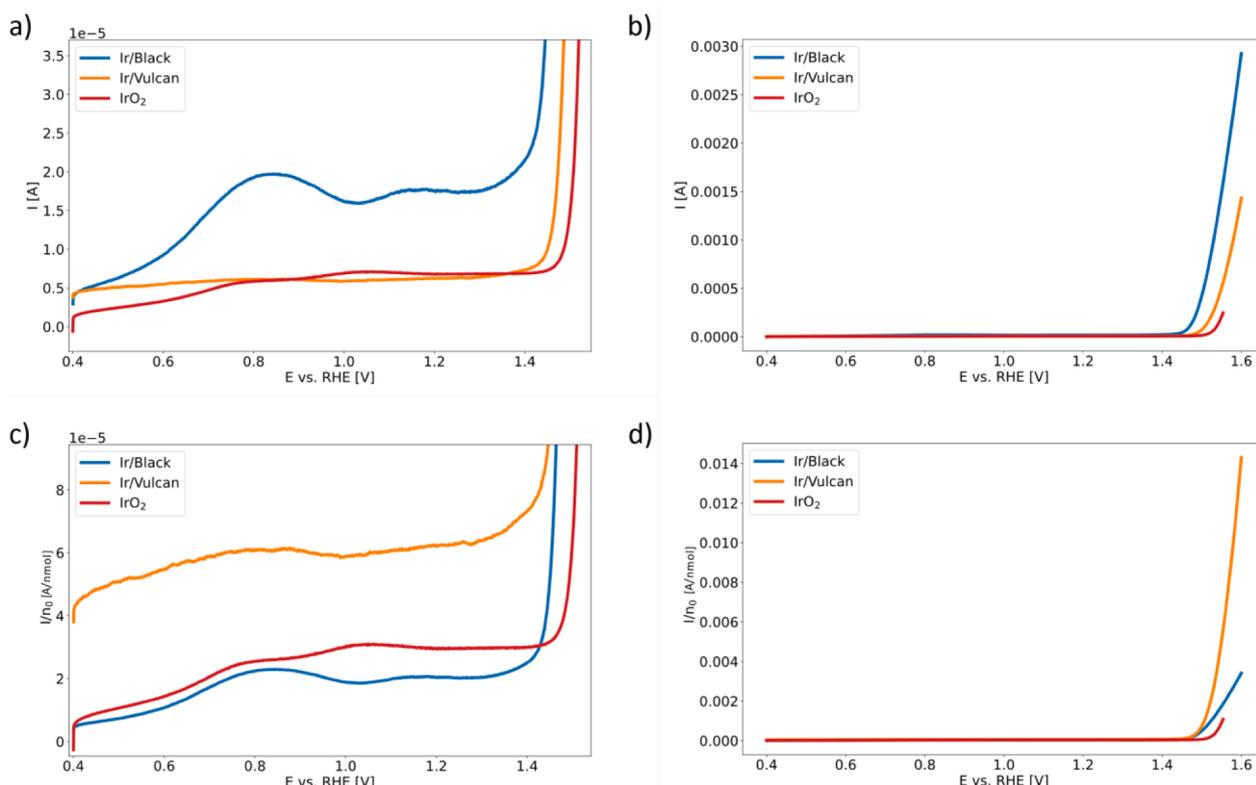
Fig. 6. A comparison between materials. Fig. 6a and b show the LSV curves without normalization, with 6a being the close-up of the region between 0.4 V and 1.45 V of Fig. 6b. Fig. 6c and d are the LSV curves normalized by the number of active sites, with Fig. 6c again being the close-up of the region found in 6d The LSVs for this image are taken when the material is at its most active (after 100 cycles for Ir Black and Ir on Vulcan, 1000 cycles for the IrO_2 sample). The LSV is taken between 0.4 V and 1.6 V, with a scan rate of 5 mV/s in 0.1 M $HClO_4$. Potentials are reported versus RHE.

active site density of 0.086 nmol/µg and 0.015 nmol/µg for Ir/Black and IrO_2, respectively.

As discussed earlier in the text, one deficiency that has occurred is a lack of consistency in the fit of the harmonics. While the kinetic parameters remain roughly the same, the number of active sites found for the studied material varies greatly between harmonics. The reduction in the number of active sites due to the process is observed for all materials studied. This inconsistency is likely due to the dispersion of parameter values demonstrated for surface-bound reactions [33,34]. This essentially suggests that different facets of the Ir nanoparticles studied behave differently under the same experimental conditions, such that our studied current is a combination of signals for each facet on our nanoparticles. Currently, this suggests that there is a frequency dependence on the number of active sites, showing that certain facets are not as well suited for OER as others. The model would need to be further optimized to fully capture the parameter dispersion. For more information on parameter dispersion, see the article by Lloyd-Laney et al. [33,34]. Other parameters also show some frequency dependence, such as the formal potential of the E1 step, being the other notable example. Again, showing the different frequency responses of different active sites.

These results show that not all materials studied are necessarily the same catalyst. By observing and then fitting our data from ACV we can determine that there are indeed kinetic differences between all the materials studied. We believe that these differences are a result of the environment of the Ir-based nanoparticles. The environment affects how adsorption to the material occurs and how it behaves kinetically. This leads us to believe that how a reactant gains access to the active site is of great importance in the development of novel electrocatalysts and that care should be taken in the development of supporting material and catalytic particles. Currently, these observations are only made by analyzing the intrinsic activities and active site density of the materials

under study, and further research is needed to better understand these phenomena.

4. Conclusion

In this work, we have shown that the presented approach of ACV together with the mechanistic fitting can be used for screening the electrochemical intrinsic properties and OER mechanism of Ir-based materials. Using this approach, we have shown that Ir-metal-based materials evolve differently from IrO_2 when subjected to activation cycling between oxidizing and reducing potentials. In particular, IrO_2 needs 1000 cycles (ATN) to reach a steady state, whereas the other two Ir analogs need only 100 (ATN). We have also shown the similarities and differences in the OER reaction pathway for both materials. We found that the OER reaction pathway is impeded by water adsorption on metallic Ir materials, while rutile oxide has kinetic limitations, but both materials have the same underlying kinetic pathway. This was demonstrated by fitting a mechanistic model to the measured response and comparing the constants found. We also used the fitted parameters to find the catalyst with the best intrinsic properties among the three studied. We compared the catalyst based on their current normalized to the number of active sites, as well as on the Ir mass-based density of active sites, and found that Ir on Vulcan performed three times better than the other two materials. Our approach can thus offer a reliable way of extracting intrinsic properties of Ir electrocatalysts.

CRediT authorship contribution statement

Ožbej Vodeb: Conceptualization, Methodology, Investigation, Formal analysis, Data curation, Writing – original draft. **Anja Lončar:** Conceptualization, Methodology, Investigation. **Marjan Bele:**

Investigation. **Armin Hrnjić:** Investigation. **Primož Jovanovič:** Writing – review & editing. **Miran Gaberšček:** Supervision, Writing – review & editing, Funding acquisition. **Nejc Hodnik:** Conceptualization, Supervision, Writing – original draft, Funding acquisition.

Declaration of Competing Interest

The authors declare that they have no known competing financial interests or personal relationships that could have appeared to influence the work reported in this paper.

Data availability

Data will be made available on request.

Supplementary materials

Supplementary material associated with this article can be found, in the online version, at doi:10.1016/j.electacta.2023.142882.

References

[1] M. Carmo, D.L. Fritz, J. Mergel, D. Stolten, A comprehensive review on PEM water electrolysis, Int. J. Hydrog. Energy (2013) 4901–4934, https://doi.org/10.1016/j.ijhydene.2013.01.151.

[2] J. Kibsgaard, I. Chorkendorff, Considerations for the scaling-up of water splitting catalysts. Nature Energy, Nature Publishing Group, 2019, pp. 430–433, https://doi.org/10.1038/s41560-019-0407-1.

[3] M.A. Hubert, L.A. King, T.F. Jaramillo, E.valuating the case for reduced precious metal catalysts in proton exchange membrane electrolyzers, ACS Energy Lett. 7 (1) (2022) 17–23, https://doi.org/10.1021/acsenergylett.1c01869.

[4] C. Minke, M. Suermann, B. Bensmann, R. Hanke-Rauschenbach, Is iridium demand a potential bottleneck in the realization of large-scale PEM water electrolysis? Int. J. Hydrog. Energy 46 (46) (2021) 23581–23590, https://doi.org/10.1016/j.ijhydene.2021.04.174.

[5] S. Cherevko, S. Geiger, O. Kasian, A. Mingers, K.J.J. Mayrhofer, Oxygen evolution activity and stability of iridium in acidic media. part 1. - metallic iridium, J. Electroanal. Chem. 773 (2016) 69–78, https://doi.org/10.1016/j.jelechem.2016.04.033.

[6] S. Cherevko, S. Geiger, O. Kasian, A. Mingers, K.J.J. Mayrhofer, Oxygen evolution activity and stability of iridium in acidic media. part 2. - electrochemically grown hydrous iridium oxide, J. Electroanal. Chem. 774 (2016) 102–110, https://doi.org/10.1016/j.jelechem.2016.05.015.

[7] D.A.J. Rand, R. Woods, Cyclic voltammetric studies on iridium electrodes in sulphuric acid solutions, J. Electroanal. Chem. Interfacial Electrochem. 55 (3) (1974) 375–381, https://doi.org/10.1016/S0022-0728(74)80431-6.

[8] E.J. Frazer, R. Woods, The oxygen evolution reaction on cycled iridium electrodes, J. Electroanal. Chem. 102 (1) (1979) 127–130, https://doi.org/10.1016/S0022-0728(79)80036-4.

[9] S. Gottesfeld, Faradaic processes at the ir/ir oxide electrode, J. Electrochem. Soc. 127 (9) (1980) 1922–1925, https://doi.org/10.1149/1.2130037.

[10] L.D. Burke, E.J.M.O Sullivan, Oxygen gas evolution on hydrous oxides — an example of three-dimensional electrocatalysis? J. Electroanal. Chem. 117 (1981) 155–160.

[11] E. Fabbri, T.J. Schmidt, Oxygen evolution reaction - the enigma in water electrolysis, ACS Catal. (2018) 9765–9774, https://doi.org/10.1021/acscatal.8b02712. American Chemical Society.

[12] P.G. Pickup, V.I. Birss, A. model for anodic hydrous oxide growth at iridium, J. Electroanal. Chem. Interfacial Electrochem. 220 (1) (1987) 83–100, https://doi.org/10.1016/0022-0728(87)88006-3.

[13] J. Geppert, P. Röse, S. Czioska, D. Escalera-López, A. Boubnov, E. Saraçi, S. Cherevko, J.D. Grunwaldt, U. Krewer, Microkinetic analysis of the oxygen evolution performance at different stages of iridium oxide degradation, J. Am. Chem. Soc. 144 (29) (2022) 13205–13217, https://doi.org/10.1021/jacs.2c03561.

[14] J. Geppert, F. Kubannek, P. Röse, U. Krewer, Identifying the oxygen evolution mechanism by microkinetic modelling of cyclic voltammograms, Electrochim. Acta 380 (2021), https://doi.org/10.1016/j.electacta.2021.137902.

[15] A.M. Bond, N.W. Duffy, S.X. Guo, J. Zhang, D. Elton, Changing the look of voltammetry, Anal. Chem. 77 (9) (2005), https://doi.org/10.1021/ac053370k.

[16] Y. Zhang, A.N. Simonov, J. Zhang, A.M. Bond, Fourier transformed alternating current voltammetry in electromaterials research: direct visualisation of important underlying electron transfer processes. current opinion in electrochemistry, Elsevier (2018) 72–81, https://doi.org/10.1016/j.coelec.2018.04.016.

[17] Bond A.M.; Mashkina E.A.; Simonov A.N. 2. A critical review of the methods available for quantitative evaluation of electrode kinetics at stationary macrodisk electrodes; 2014.

[18] S.A. Bonke, A.M. Bond, L. Spiccia, A.N. Simonov, Parameterization of water electrooxidation catalyzed by metal oxides using fourier transformed alternating current voltammetry, J. Am. Chem. Soc. 138 (49) (2016) 16095–16104, https://doi.org/10.1021/jacs.6b10304.

[19] L. Gundry, S.X. Guo, G. Kennedy, J. Keith, M. Robinson, D. Gavaghan, A.M. Bond, J. Zhang, Recent advances and future perspectives for automated parameterisation, bayesian inference and machine learning in voltammetry, Chem. Commun. 57 (15) (2021) 1855–1870, https://doi.org/10.1039/d0cc07549c.

[20] P. Virtanen, R. Gommers, T.E. Oliphant, M. Haberland, T. Reddy, D. Cournapeau, E. Burovski, P. Peterson, W. Weckesser, J. Bright, S.J. van der Walt, M. Brett, J. Wilson, K.J. Millman, N. Mayorov, A.R.J. Nelson, E. Jones, R. Kern, E. Larson, C. J. Carey, \.Ilhan Polat, Y. Feng, E.W. Moore, J. VanderPlas, D. Laxalde, J. Perktold, R. Cimrman, I. Henriksen, E.A. Quintero, C.R. Harris, A.M. Archibald, A.H. Ribeiro, F. Pedregosa, P. van Mulbregt, SciPy 1.0 contributors. scipy 1.0: fundamental algorithms for scientific in python, Nat. Methods 17 (2020) 261–272, https://doi.org/10.1038/s41592-019-0686-2.

[21] W.H. Press, S.A. Teukolsky, W.T. Vetterling, B.P. Flannery, N.umerical Recipes, 3rd Ed., Cambridge university press, Cambridge, 2011 https://doi.org/10.1017/cbo9780511599798.031.

[22] B.E. Conway, B. Barnett, H. Angerstein-Kozlowska, B.V. Tilak, A. surface-electrochemical basis for the direct logarithmic growth law for initial stages of extension of anodic oxide films formed at noble metals, J. Chem. Phys. 93 (11) (1990) 8361–8373, https://doi.org/10.1063/1.459319.

[23] J. Mozota, B.E. Conway, Surface and bulk processes at oxidized iridium electrodes—i. monolayer stage and transition to reversible multilayer oxide film behaviour, Electrochim. Acta 28 (1) (1983) 1–8, https://doi.org/10.1016/0013-4686(83)85079-8.

[24] B.E. Conway, J. Mozota, Surface and bulk processes at oxidized iridium electrodes—ii. conductivity-switched behaviour of thick oxide films, Electrochim. Acta 28 (1) (1983) 9–16, https://doi.org/10.1016/0013-4686(83)85080-4.

[25] A. BalaKrishnan, N. Blanc, U. Hagemann, P. Gemagami, K. Wonner, K. Tschulik, T. Li, Direct detection of surface species formed on iridium electrocatalysts during the oxygen evolution reaction, Angew. Chem. Int. Ed. 60 (39) (2021) 21396–21403, https://doi.org/10.1002/anie.202106790.

[26] N. Sivasankar, W.W. Weare, H. Frei, Direct observation of a hydroperoxide surface intermediate upon visible light-driven water oxidation at an ir oxide nanocluster catalyst by rapid-scan ft-ir spectroscopy, J. Am. Chem. Soc. 133 (33) (2011) 12976–12979, https://doi.org/10.1021/ja205300a.

[27] C. Bozal-Ginesta, R.R. Rao, C.A. Mesa, X. Liu, S.A.J. Hillman, I.E.L. Stephens, J. R. Durrant, Redox-state kinetics in water-oxidation irox electrocatalysts measured by operando spectroelectrochemistry, ACS Catal. 11 (24) (2021) 15013–15025, https://doi.org/10.1021/acscatal.1c03290.

[28] G. Koderman Podboršek, A.R. Kamšek, A. Lončar, M. Bele, L. Suhadolnik, P. Jovanovič, N. Hodnik, Atomically-resolved structural changes of ceramic supported nanoparticulate oxygen evolution reaction Ir catalyst, Electrochim. Acta 426 (2022), https://doi.org/10.1016/j.electacta.2022.140800.

[29] M. Bele, K. Stojanovski, P. Jovanovič, L. Moriau, G. Koderman Podboršek, J. Moškon, P. Umek, M. Sluban, G. Dražič, N. Hodnik, M. Gaberšček, Towards stable and conductive titanium oxynitride high-surface-area support for iridium nanoparticles as oxygen evolution reaction electrocatalyst, ChemCatChem 11 (20) (2019) 5038–5044, https://doi.org/10.1002/cctc.201901487.

[30] C. Daiane Ferreira Da Silva, F. Claudel, V. Martin, R. Chattot, S. Abbou, K. Kumar, I. Jiménez-Morales, S. Cavaliere, D. Jones, J. Rozière, L. Solà-Hernandez, C. Beauger, M. Faustini, J. Peron, B. Gilles, T. Encinas, L. Piccolo, F.H. Barros De Lima, L. Dubau, F Maillard, Oxygen evolution reaction activity and stability benchmarks for supported and unsupported IrOxelectrocatalysts, ACS Catal. 11 (7) (2021) 4107–4116, https://doi.org/10.1021/acscatal.0c04613.

[31] H.N. Nong, L.J. Falling, A. Bergmann, M. Klingenhof, H.P. Tran, C. Spöri, R. Mom, J. Timoshenko, G. Zichittella, A. Knop-Gericke, S. Piccinin, J. Pérez-Ramírez, B. R. Cuenya, R. Schlögl, P. Strasser, D. Teschner, T.E. Jones, Key role of chemistry versus bias in electrocatalytic oxygen evolution, Nature 587 (7834) (2020) 408–413, https://doi.org/10.1038/s41586-020-2908-2.

[32] S.M. Alia, B. Rasimick, C. Ngo, K.C. Neyerlin, S.S. Kocha, S. Pylypenko, H. Xu, B. S. Pivovar, Activity and durability of iridium nanoparticles in the oxygen evolution reaction, J. Electrochem. Soc. 163 (11) (2016) F3105–F3112, https://doi.org/10.1149/2.0151611jes.

[33] H.O. Lloyd-Laney, M.J. Robinson, A.M. Bond, A. Parkin, D.J. Gavaghan, A. spotter's guide to dispersion in non-catalytic surface-confined voltammetry experiments, J. Electroanal. Chem. 894 (2021), https://doi.org/10.1016/j.jelechem.2021.115204.

[34] Rowe G.K.; Carter M.T.; Richardson J.N.; Murray R.W. Consequences of kinetic dispersion on the electrochemistry of an adsorbed redox-active monolayer; 1995; Vol. 11. https://pubs.acs.org/sharingguidelines.